Tunable Near UV Microcavity OLED Arrays: Characterization and Analytical Applications

Eeshita Manna, Fadzai Fungura, Rana Biswas, Joseph Shinar, and Ruth Shinar**

A new approach is demonstrated to fabricate narrow-band emission near-UV microcavity OLEDs (μcOLEDs) with peak emission at ≈385 nm, in near-perfect alignment with the narrow primary 385 nm absorption band of Pt octaethylporphyrin dye, using 4,4′-bis(9-carbazolyl)-1,1′-biphenyl (CBP) as the emissive layer. Although OLEDs have been extensively operated at optical wavelengths, only few have achieved near-UV emission. Yet there is a growing need for portable compact narrow-band near UV sources for many biomedical and forensic applications. A microcavity effect, due to metallic electrodes enclosing an optical cavity, is employed to achieve the desired narrow peak emission. An Al/Pd bi-layer anode enables attaining a turn on voltage of 3.8 V and a 4,4′-cyclohexylidenebis [*N*,*N*-bis (4-methylphenyl) benzenamine] (TAPC) layer improves electron-hole recombination in the emissive layer. The fabricated μcOLED is efficiently used as the excitation source in a structurally integrated all-organic oxygen sensor. Moreover, a CBP-based combinatorial array of μcOLED pixels is fabricated by varying the thickness of the organic layers to obtain nine sharp, discrete emission peaks from 370 to 430 nm, employed in an all-organic on-chip spectrophotometer. The photodetectors are based on P3HT:PCBM (poly(3-hexylthiophene):[6,6]-phenyl-C_{60}-butyric acid methyl ester) or the more sensitive PTB7:PCBM (PTB7 is polythieno [3,4-b]-thiophene-co-benzodithiophene). Simulations of the OLEDs' emission are used for analysis of the experimental data, assisting in device fabrication.

1. Introduction

Organic light emitting diodes' (OLEDs') attributes include many promising features such as compatibility with simple and flexible substrates[1–5] and easily adaptable size and design.[6,7] As such, they are uniquely simple to integrate with other components to generate compact devices for optical analytical applications.[3,4,8–12] Indeed, the unique characteristics of OLEDs resulted in their incorporation in various sensing schemes.[13–18] As an example, OLEDs were used as excitation sources in optical gas and liquid phase (bio)chemical sensors, including O_2 sensors.[3,8–12,19] The latter play a crucial role in e.g., food packaging, medical testing, and biological applications, including cell cultivation, marine biology, and enzymatic biosensing.[20–22] OLEDs, together with organic photodetectors (OPDs), address a growing need for more compact, field-deployable integrated devices, though challenges associated with such all-organic platforms still exist.[3,13]

In attempts to improve OLEDs for solid-state lighting and display applications, devices with many different configurations were explored.[23,24] The focus of OLED R&D, however, has been mainly on devices emitting in the visible range.[24] Significantly less research has been aimed at developing efficient OLEDs emitting in the near UV or near IR regions.[25–27] Yet efficient deep-blue/near UV OLEDs and arrays with pixels emitting at different wavelengths in this range are of strong interest for analytical applications.[3,10] For these applications, microcavity OLEDs (μcOLEDs) are advantageous as the otherwise broad electroluminescence (EL) band of the OLED[3] narrows and can be tailored to a desired peak emission wavelength $\lambda_{\max}$ by tuning the cavity modes.[28–30] Moreover, the sharper OLED emission bands minimize interference with the photoluminescence (PL) of sensing probes. In addition, the microcavity structure allows fabrication of a combinatorial array of OLED pixels with tunable narrower emission bands on a common, small-size substrate,[30] which can be adapted as an on-chip spectrometer and for simultaneous detection of multiple analytes.

The optical O_2 sensor comprises three major components: the excitation source, the sensor film, and the photodetector (PD). Sensing is based on monitoring the PL whose intensity and decay time depend on the dose of the quenching element.[3,8–12] PL quenching occurs via O_2–dye collisions in a dynamic process;[31] ideally it is described by the Stern–Volmer (SV) equation[3,8–11]

$$\frac{I_0}{I} = \frac{\tau_0}{\tau} = 1 + K_{sv}[O_2] \tag{1}$$

E. Manna, F. Fungura, Prof. R. Biswas, Prof. J. Shinar
Ames Laboratory – USDOE
Ames, IA 50011-3020, USA
E-mail: jshinar@iastate.edu
E. Manna, Prof. R. Biswas, Prof. R. Shinar
Electrical and Computer Engineering Department
Iowa State University
Ames, IA 50011, USA
E-mail: rshinar@iastate.edu
F. Fungura, Prof. R. Biswas, Prof. J. Shinar
Physics and Astronomy Department
Iowa State University
Ames, IA 50011-3160, USA
Prof. R. Biswas, Prof. R. Shinar
Microelectronics Research Center
Iowa State University
Ames, IA 50011, USA

DOI: 10.1002/adfm.201403313

where I_0 and τ_0 are the PL intensity and decay time, respectively, at 0% oxygen, and I and τ are the values in the presence of oxygen. K_{SV} is the SV constant. The sensitivity S is defined as τ_0/τ(100% O_2) or I_0/I(100% O_2).

Several approaches have been developed to increase the sensitivity of the sensor as well as the PL intensity. Pt octaethylporphyrin (PtOEP) embedded in a polystyrene (PS) matrix is often used, but PS is only moderately permeable to oxygen.[3] Studies show that polyethylene glycol (PEG) blended with PS (PEG:PS) at ratios of 1:9 to 1:4 and PtOEP:PEG:PS sensing films enhance OLED outcoupling and the PL intensity, respectively.[8,32]

In this work novel near UV 4,4′-bis(9-carbazolyl)-1,1′-biphenyl (CBP)-based µcOLEDs were fabricated by using, inter alia, Al/Pd cathodes, and they were successfully used for improved O_2 sensing. Additionally, a combinatorial array of tunable CBP-based µcOLEDs emitting in the 370–430 nm range was used in an on-chip spectrometer. The O_2 sensor was a structurally integrated all-organic OLED/sensing film/OPD device. The OLED's peak emission was tuned to 385 nm, where the PtOEP has a strong absorption peak.[33] The sensing film was a PtOEP:PEG:PS blend; it was drop cast on the back side of the OLED's glass substrate. The OPD, in the front detection configuration,[3,8] was based on the standard P3HT:PCBM (where P3HT is poly(3-hexyl thiophene) and PCBM is phenyl-C_{61}-butyric acid methyl ester) or a more sensitive one, which was based on polythieno [3,4-b]-thiophene-co-benzodithiophene (PTB7). The choice of the µcOLED eliminates the issue related to the OLED's EL tail that is otherwise detected by the OPD, generating an interfering background. The blend sensing film results in enhanced PL signals.[8] The utility of the combinatorial array of the OLED pixels is demonstrated by using it to measure the absorbance spectrum of an Alexa Fluor 405 film. The 370–430 nm range presented here is a step toward expansion of the range covered by µcOLED pixels emitting in the 493–639 nm visible range,[30] and the integration with an OPD, first undertaken here for the on-chip OLED-based spectrometer, presents a step toward achieving a compact, economical spectrometer.

Simulations of emission from OLEDs, which assisted in device design, were performed with our scattering matrix approach, described previously.[34]

2. Results and Discussion

2.1. µcOLED Design

Due to strong optical absorption by ITO[35] and most common metals in the UV, the standard near-UV OLED and the µcOLEDs, where a very thin metal layer is used as the semitransparent anode, have a high loss at the electrode/organic interface, which results in reduced device efficiency. Thin Ag metal has been extensively used as a semitransparent anode in µcOLEDs emitting in the visible because its high reflectance and low absorption in that region provide a very good lossless microcavity.[28,30,36] However below 400 nm, the absorption of silver increases rapidly and its reflectance decreases.[37,38] Despite being lossy, Al is well suited for fabricating a strong optical near UV microcavity due to its uniform reflectance in this wavelength range. **Figure 1** shows the irradiance R versus voltage for CBP-based standard and µcOLEDs of the structure anode/MoO_x (5 nm)/CBP (25 nm)/bathophenanthroline (BPhen) (35 nm)/LiF/Al with three different anodes: ≈140 nm ITO,[11] 25 nm Ag, and 15 nm Al.

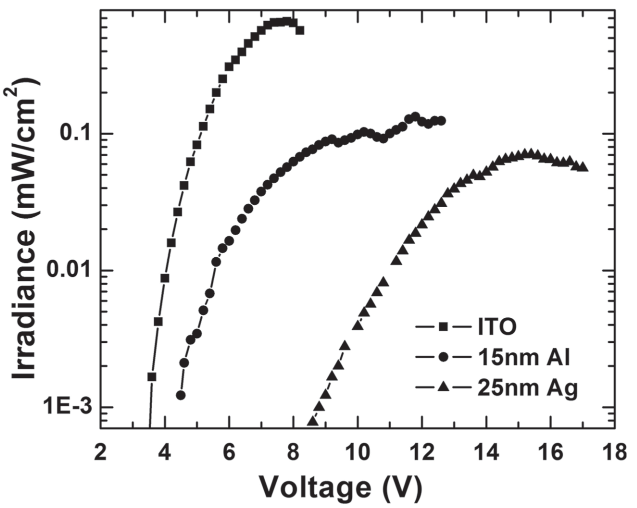

Figure 1. Irradiance R versus V for UV CBP OLEDs with ITO, Ag, or Al anodes.

One of this work's goals was to obtain an easy-to-fabricate anode that provides a good microcavity and a low turn on voltage for the near-UV OLED. The work function of Al is ≈−4 to −4.2 eV, so to improve hole injection, a very thin layer of palladium was added. Adding just 5 nm of Pd on top of the Al anode improves the hole injection due to Pd's deeper Fermi level (≈−5.2 to −5.6 eV) without significantly affecting the EL full width at half maximum (FWHM), which is 25 nm, with the EL peak red-shifting by ≈5 nm (from 382 to 387 nm). The addition of the Pd layer also prevents the formation of a thin insulating Al oxide layer. **Figure 2** compares R and current density (J) versus voltage for devices with Al versus Al/Pd anodes.

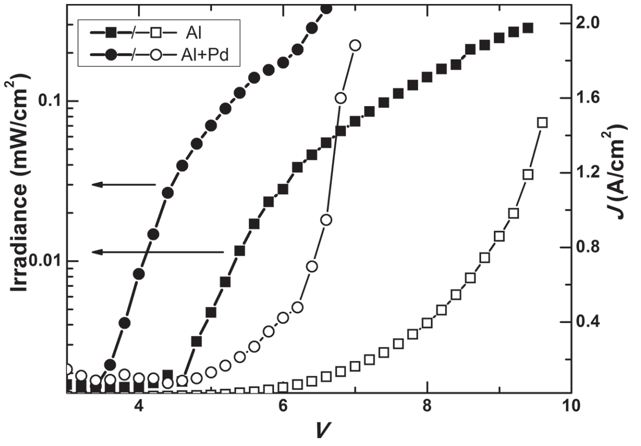

Figure 2. R and J versus V for µcOLEDs with Al or bi-layer Al/Pd anodes with the structure anode/MoO_x (5 nm)/CBP (25 nm)/BPhen (35 nm)/LiF/Al.

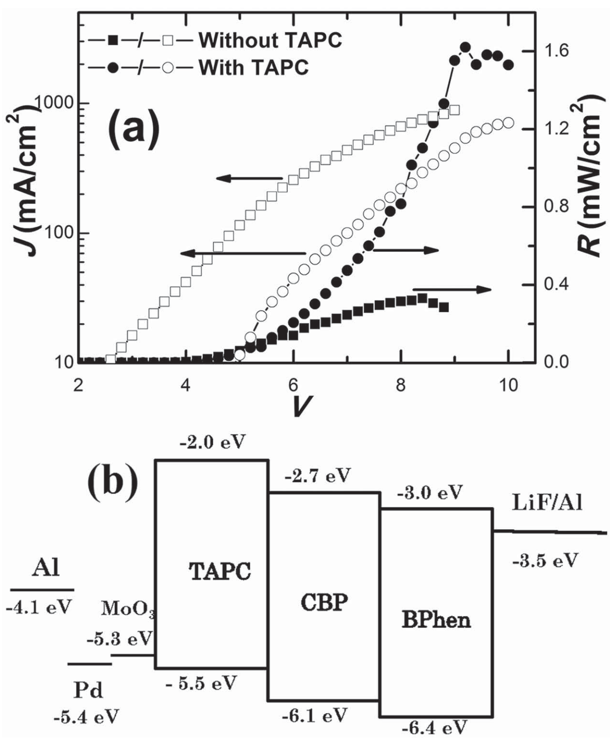

Figure 3. a) *J–R–V* curves of OLEDs with and without a TAPC hole transport layer. b) The energy level diagram of the device.

In the μcOLEDs, the thickness of the MoO_x layer is not sufficient to prevent exciton quenching by the metal anode. Additionally, though CBP has a relatively high electron mobility $\mu_e \approx 3 \times 10^{-4}$ cm^2 V^{-1}s^{-1}, it is still much lower than the hole mobility $\mu_h \approx 2 \times 10^{-3}$ cm^2 V^{-1}s^{-1}, so charge balance in the device needs improvement. Device performance indeed improved when we added a 20 nm 4,4′-cyclohexylidenebis [*N,N*-bis (4-methylphenyl) benzenamine] (TAPC) layer on the MoO_x, where the anode was Al, and 30 nm (optimized thickness) of TAPC for the device with the ITO anode. The improvement is likely due to reduced exciton quenching at the anode in the microcavity device and excellent electron and exciton blocking due to TAPC's shallow LUMO level (≈–2.0 eV). **Figure 3** shows the *J–R--V* characteristics of μcOLEDs with and without TAPC as a hole transporting layer (HTL), as well as the energy level diagram of the devices. The external quantum efficiency (EQE) without the TAPC layer is very low. In contrast, the EQE of the devices with TAPC is about 0.2%, which is comparable to previous reports on conventional UV OLEDs.[25,27] The charge imbalance in the device may be associated with the higher hole mobility of CBP (×10 larger than the electron mobility), which can result in accumulation of holes near the CBP/BPhen interface in the absence of TAPC. This charge accumulation likely quenches excitons formed near that interface.[39] Adding a TAPC layer may reduce the exciton quenching by improving charge balance in the device.

We note that the reduced current with added TAPC stems from an increase in the resistance, which increases with increasing TAPC thickness.

2.2. Gas-Phase Oxygen Sensing

Four different PtOEP-doped sensing films were evaluated for achieving the largest PL intensity and sensitivity first with a photomultiplier tube (PMT) in a back detection configuration. The four sensing films are low M_w PS (45 000), high M_w PS (288 000), 1:9 PEG:high M_w PS, and 1:4 PEG:high M_w PS. **Figure 4** shows the PL decay signal for each sensing film following application of a 1 ms voltage pulse to the OLED excitation source. As seen, the PtOEP-doped 1:9 PEG:PS film shows the highest PL intensity. Figure 4 shows also the largely linear SV plots of τ_0/τ versus $[O_2]$ with R^2 values of 0.991, 0.987, 0.983, and 0.998, respectively. The 1:9 PEG:PS film shows the best performance with the highest PL intensity and detection sensitivity $S = 20.4$. The results are in good agreement with the OLED outcoupling and PL intensity enhancement reported by Liu et al.[8,32] The scattering centers on the surface and in the bulk of the 1:9 PEG:PS film increase light absorption and hence the PL.[8] Moreover, the dye–O_2 interaction is likely increased due to the increased surface area of the sensing film, which increases *S*.

2.3. Integration with an Organic Photodetector

Standard and microcavity green tris(8-hydroxy quinoline) Al (Alq_3)-based OLEDs (≈530 nm peak emission) were used successfully for O_2 and related sensing applications.[8–11] However,

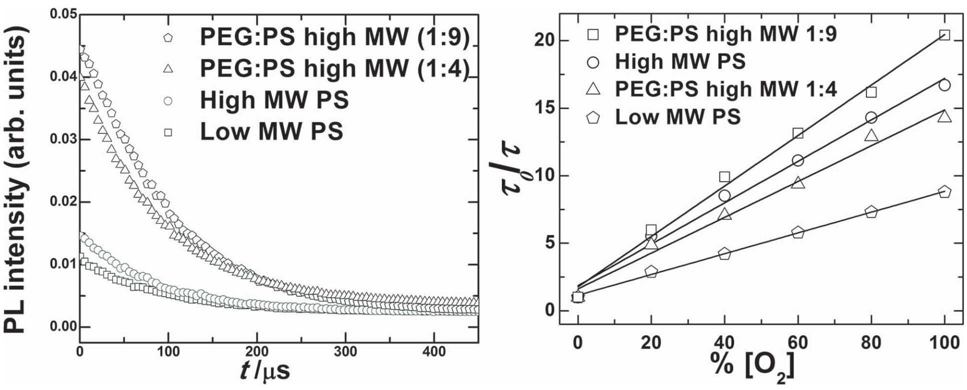

Figure 4. PL decay curves at 0% O_2 (left) and SV plots (right) with pulsed OLED excitation using different sensing films.

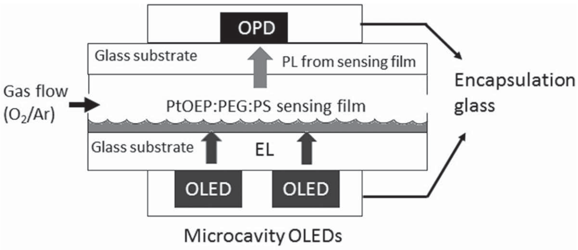

Figure 5. Schematics of the integrated all-organic sensor. (not to scale)

when replacing the PMT with an integrated OPD, the [O_2] range that can be detected is limited.[8,40] As the absorption of PtOEP (or the Pd analog PdOEP) is stronger in the near UV region (≈385–395 nm), a standard near UV[11] or μcOLED can serve as a very efficient excitation source. **Figure 5** shows the schematics of the integrated all-organic sensor. **Figure 6**a shows the SV plots for all-organic O_2 sensors using a PTB7-based OPD with a power conversion efficiency (PCE) of 6.2%. These plots show linear SV relations and the use of the UV μcOLED enabled increased dynamic range with the OPD. We note that with the green μcOLEDs in conjunction with an OPD the signal-to-noise was relatively poor even in the low [O_2] range, unlike the situation with the UV μcOLED. The PTB7-based OPD is preferably chosen for this experiment over the standard P3HT:PCBM-based OPD due to its higher sensitivity in the long wavelength range. Figure 6b compares the EQE of both OPDs along with the EL of the UV μcOLED and the PL of the sensing film.

2.4. Near-UV Spectrophotometer

2.4.1. Measurements

The resonant wavelength of an optical cavity is described by $m\lambda_r = 2\Sigma n_i(\lambda)L_i\cos\theta$, where λ is the resonant wavelength of the mth mode, and n_i and L_i are the refractive index and thickness of the ith layer, respectively. The thickness of the optical medium determines the cavity mode or the normal emission of a μcOLED. Using CBP-based microcavity structures, it was possible to tune the emission wavelength producing nine different discrete and relatively sharp peaks ranging from 370 to 430 nm on a common substrate. The combinatorial array was fabricated by varying the thickness of the CBP and BPhen layers. The structure of the devices was 15 nm Al/5 nm MoO_3/20 nm TAPC/x nm CBP/y nm BPhen/1 nm LiF/Al, where $15 \leq x \leq 30$ nm and $25 \leq y \leq 40$ nm. **Figure 7**a shows the EL spectra of these devices. The FWHM of these bands ranged from 24 to 48 nm, with the broadening of the EL spectrum at longer wavelengths due to the shape of the reference (cavity-free) CBP EL spectrum across this wavelength range (Figure 7(a)). All these devices exhibit comparable J–R–V characteristics with $R \approx 0.8$ mW cm^{-2} at $J \approx 1$ A cm^{-2}, except for the thinnest device that showed a slightly reduced R.

Figure 7b shows the schematics of the all-organic on-chip spectrometer. Figure 7c shows the absorption spectrum of an Alexa fluor 405 film using this all-organic on-chip spectrometer with the P3HT:PCBM-based OPD. As seen, the measured absorption is in good agreement with that of a reference measurement using the Ocean Optics spectrometer. The current near UV array expands the range of the on-chip spectrophotometer described by Liu et al. from the visible[30] to shorter wavelengths. The Alexa fluor 405 dye was chosen to show the potential of the all-organic on-chip spectrometer in biological applications, as this dye is extensively used in biological fluorescence imaging. The film (≈500–750 nm thick) was made from 0.1 mg mL^{-1} dye in water. Since the standard concentration of Alexa fluor 405 used in imaging is 0.5 mg mL^{-1},[41] the integrated spectrometer is promising for various future sensing/imaging applications.

2.4.2. Simulations

Simulations of the OLEDs' emission were performed with our scattering matrix approach described previously.[34] In this approach Maxwell's equations are solved in Fourier space, i.e., within a plane wave basis for the OLED architecture that contains emissive sources within the OLED. The OLED is composed of layers stacked in the z direction. In each layer of the OLED stack, the materials are represented by realistic frequency dependent absorptive dielectric functions obtained from experimental measurements of Al,[42] MoO_x,[43] and ITO.[37] The simulations are performed with all layers being planar in

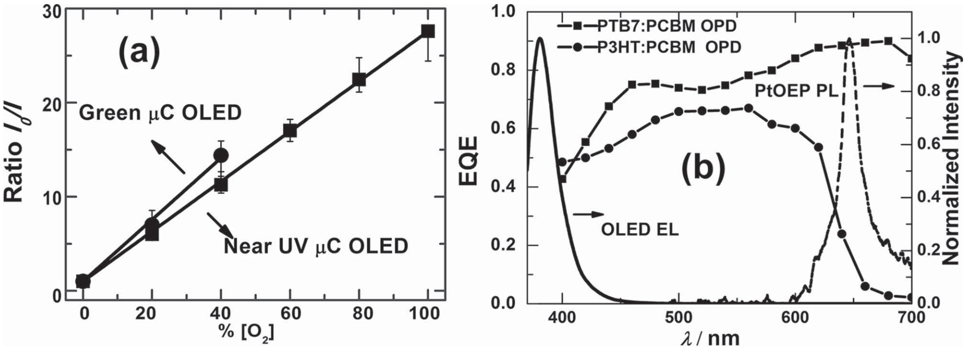

Figure 6. a) SV relation in oxygen sensing with a green (circles) or UV-μcOLED (squares) as the excitation source and PTB7-based OPD. b) EQE of P3HT:PCBM (green circles) and PTB7:PCBM (black squares) OPDs; the EL of the UV μcOLED (violet; ≈385 nm peak emission), and the normalized PL of the 1:9 PtOEP:PEG:PS sensing film (red; ≈645 nm) are also shown.

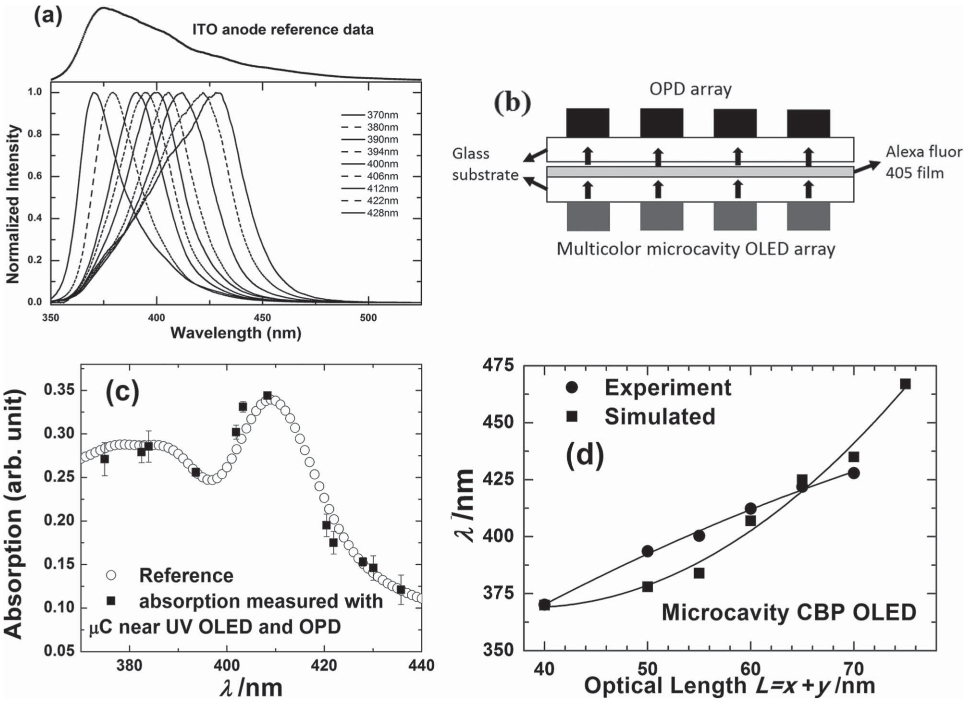

Figure 7. a) EL spectra of OLEDs of the structure 15 nm Al/5 nm MoO_3/20 nm TAPC/CBP/BPhen/1 nm LiF/Al with different CBP and BPhen layer thickness of 15–30 nm and 25–40 nm, respectively. b) Schematics of the all-organic on-chip spectrometer (not to scale). c) Absorption of an Alexa fluor 405 film on glass, measured with the near UV microcavity OLEDs and the ITO/PEDOT:PSS /P3HT:PCBM /Ca/Al photodetector (squares) and with the ocean optics system (circles). d) Comparison of the experimental and simulated peak emission wavelengths versus the optical length L. The lines are smooth fits to the simulated and experimental points.

the (x, y) plane as in the experiment. However, this approach is more general allowing the layers to have a periodic structure in the (x, y) direction with a repeat vector $\mathbf{R} = n_1\mathbf{a}_1 + n_2\mathbf{a}_2$, where the primitive lattice vectors are $\mathbf{a}_1$ and $\mathbf{a}_2$. This general formalism allows for the investigation of outcoupling of trapped modes using periodic microlens structures or grating structures, which is an important aspect for later work.

ITO-Control OLED: We first determined the thickness of the ITO layer on the glass substrates, by measuring the transmission and reflectance of ITO-coated glass and comparing these to simulated reflectance and transmission. The measured transmission exhibited 85%–90% transmission over most of the optical spectrum, with a broad peak near 450 nm and a sharp dip at shorter wavelengths, in conjunction with a minimum reflectance near 450 nm, and increasing reflectance at shorter wavelengths. These features were best modeled by an ITO thickness of 110 nm. Larger ITO thicknesses shifted the broad peak position to longer wavelength, whereas thinner ITO moved this peak feature to shorter wavelength. Using this ITO thickness we simulated the emission from the control ITO-based structure composed of glass ITO/MoO_3 (7 nm)/TAPC (20 nm)/CBP (15 nm)/BPhen (25 nm)/LiF (1 nm)/Al. A single wavelength-dependent refractive index $n + ik$ was used for all the organic layers taken from ellipsometry measurements of organic materials,[41] since the optical properties of each individual organic constituent were not available. This approximation may be justified given the small variations expected for n of the individual organic materials. It successfully simulated the measured emission that peaked at 375 nm.

Microcavity OLEDs: Next we simulated the OLED stack composed of Al (15 nm)/MoO_3 (5 nm)/TAPC (20 nm)/CBP (x nm)/BPhen (y nm)/LiF/Al (100 nm), utilizing available n and k values.[44] We utilized an emissive source at the CBP/BPhen interface. First, the emitted intensity E_0 (λ) below the glass was simulated assuming the source inside the OLED has a featureless emission profile. This approach yields the dependence of the emission on the optical cavity length without added assumptions on how the emissive source emits at different wavelengths. Since x and y were varied to tune the microcavity wavelength, we found it convenient to plot the emission peak as a function of the optical length $L = x + y$ (as distinct from the full optical microcavity length, which extends into the bottom and top Al electrodes[30]). The emission intensity exhibits a peak value that increases as the optical cavity length is increased (Figure 7(d)). The position of the shortest wavelength emission at 370 nm (x = 15 nm; y = 25 nm; L = 40 nm, the shortest optical length) is in excellent agreement with simulation. The longer optical cavities (L = 60 nm with x = 25 nm, y = 35 nm and L = 65 nm with x = 30 nm, y = 35 nm) also exhibit good agreement of the peak emission wavelengths between experiment and simulation (Figure 7d). Simulations at intermediate L underestimated the positions of the peak wavelengths relative to the experiment. The measurements displayed an almost linear increase of peak wavelengths with L, whereas the simulation showed a more quadratic dependence. As found in our earlier work[30] the complete optical microcavity length must include contributions from the penetration of fields in the Al cathode and anode, and is larger than the simple optical lengths within the electrodes.

The foregoing results suggest that the source CBP emission profile $I_s(\lambda)$ is strongly wavelength dependent. Accordingly, we used the experimentally measured emission $E_{exp}(\lambda)$ and the simulated emission intensity $E_0(\lambda)$ to obtain the emission profile of the emissive CBP species $I_s(\lambda)$ from $E_{exp}(\lambda) = E_0(\lambda)^*I_s(\lambda)$. We obtain the source profile $I_s(\lambda)$ to be sharply peaked near 370 nm for short optical lengths (L = 40 nm) and a broad profile with a peak at 425 nm at the longest optical length (L = 70 nm) in accordance with the experimental results of Figure 7a. As the microcavity length increases, the CBP emission broadens and red shifts significantly, as would be expected for strong microcavity effects.

3. Summary and Conclusions

We demonstrated simple fabrication and characterization of improved near UV microcavity OLEDs, with peak emission at ≈385 nm, using CBP as the emitting layer. BPhen and TAPC layers at the cathode and anode, respectively, strongly enhanced device performance improving electron-hole recombination in the emitting layer. A relatively low turn-on voltage of ≈3.8 V—only 0.58 V above the 385 nm photon energy—was achieved via the use of an Al/Pd bi-layer anode, rather than Al only. We also demonstrated the structural integration of this device with an OPD to generate an all-organic compact O_2 sensor. The use of the near UV µcOLED improved the sensor performance in comparison to the previously used green µcOLED for probe excitation, where the $[O_2]$ dynamic range was limited. In addition, we tuned this near UV microcavity device to produce a multicolor µcOLED array by gradually changing the thickness of the CBP and BPhen layers. This array was utilized in an all-organic spectrometer on a chip for measuring the absorption spectrum of an Alexa fluor 405 dye film. Two different OPDs, i.e., P3HT:PCBM- and PTB7:PCBM-based, were utilized; the latter improved the sensing performance. Simulations based on the scattering matrix approach were in good agreement with the experimental results and contributed to device fabrication.

4. Experimental Section

Materials: PtOEP, PS (molecular weight $M_w \approx 45\,000$ and 288 000) and PEG ($M_w \approx 1000$) were used to prepare the sensing films. The dye was purchased from H. W. Sands and PS and PEG were purchased from Sigma–Aldrich. MoO_3, the hole injection material, was purchased from Sterm Chemicals, TAPC, the hole transport and electron-blocking material, and CBP, the emitting material, were purchased from Luminescence Technology Corporation. The hole- and exciton-blocking material BPhen was purchased from Sigma–Aldrich and used as the electron transport material. Alexa fluor 405 dye was purchased from Life Technologies.

OLED Fabrication: OLEDs were fabricated on cleaned and UV-ozone treated glass substrates inside a thermal evaporation chamber with a base pressure of $\approx 10^{-6}$ mbar within a glovebox. Al electrodes and all organic materials were deposited by thermal evaporation. The Al cathode was deposited through a shadow mask containing either 1.5 mm diameter circular holes or 3 mm wide stripes. The combinatorial array for the spectrometer was fabricated by varying the thickness of organic layers using a sliding shutter. The devices were all encapsulated using a glass cover bonded to the glass substrate with epoxy.

Film Fabrication: PtOEP, PS, and PEG were dissolved in 1 mL toluene at different weight ratios to generate solutions of 1:40 PtOEP:PS ($M_w \approx 45\,000$), 1:40 PtOEP:PS ($M_w \approx 288\,000$), 1:4:36 PtOEP:PEG:PS ($M_w \approx 288\,000$), and 1:8:32 PtOEP:PEG:PS ($M_w \approx 288\,000$). The sensing films were prepared by drop-casting 200 µL of the solution on the back side of OLED glass substrates. The OLEDs (excitation source) were driven by a pulse generator (Avtech AV-1011B) generating 1 ms pulses at a rate of 50 Hz. Various concentrations of oxygen were generated by mixing high purity Ar and O_2, using mass flow controllers, at a constant flow rate. The Alexa fluor 405 films, 500–750 nm thick, were made from 0.1 mg mL^{-1} dye in water and baked at 120 °C for two h.

Measurements: OLED Characterization: Characterization of the OLEDs was done using a Keithley 2400 source meter to apply a voltage and measure the current. A Thorlab PM100 power meter was used for measuring the irradiance. The EL spectra were obtained using an Ocean Optics CHEM2000 spectrometer. The raw spectra were obtained in the "SCOPE" mode, but were corrected to the radiometrically calibrated mode; the spectra shown are the corrected spectra.

PL and Absorption Measurements: The PL decay curves of the sensing film at different oxygen concentrations were monitored by a Hamamatsu R6060 photomultiplier tube (PMT). The PL intensity of the 1:4:36 PtOEP:PEG:PS sensing film was monitored with standard P3HT:PCBM and PTB7:PCBM OPDs and the current from the detector was measured by a Keithley 2400 source meter. In the latter case the OLED was driven by a constant voltage generated by a KEPCO (Abc-125 1 dm) power supply.

Acknowledgements

Ames Laboratory is operated by Iowa State University for the US Department of Energy (USDOE) under Contract No. DE-AC 02–07CH11358. The research was partially supported by Basic Energy Sciences, Division of Materials Science and Engineering, USDOE. This research used resources of the National Energy Research Scientific Computing Center, which is supported by the Office of Science of the USDOE under Contract No. DE-AC02–05CH11231. The authors also thank Chun Xu for computational programs.

Received: September 22, 2014
Revised: December 2, 2014

---

[1] S. Purandare, E. F. Gomez, A. J. Steckl, *Nanotechnology* **2014**, *25*, 094012.
[2] H. H. Kim, H. J. Kim, B. J. Choi, Y. S. Lee, S. Y. Park, L. S. Park, *Mol. Cryst. Liq. Cryst.* **2013**, *584*, 153.
[3] J. Shinar, R. Shinar, *J. Phys. D: Appl. Phys.* **2008**, *41*, 133001.
[4] T. Mayr, T. Abel, E. Kraker, S. Köstler, A. Haase, C. Konrad, M. Tscherner, B. Lamprecht, *Proc. Eng.* **2010**, *5*, 1005.
[5] T. H. Han, Y. Lee, M. R. Choi, S. H. Woo, S. H. Bae, B. H. Hong, J. H. Ahn, T. W. Lee, *Nat. Photonics* **2012**, *6*, 105.
[6] K. Hoshino, T. Hasegawa, K. Matsumoto, I. Shimoyama, *Sens. Act. A* **2006**, *128*, 339.
[7] J. W. Park, D. C. Shin, S. H. Park, *Semicond. Sci. Technol.* **2011**, *26*, 034002.
[8] R. Liu, T. Xiao, W. Cui, J. Shinar, R. Shinar, *Anal. Chim. Acta* **2013**, *778*, 70.
[9] Y. Cai, R. Shinar, Z. Zhou, J. Shinar, *Sens. Act. B* **2008**, *134*, 727.
[10] Z. Zhou, R. Shinar, B. Choudhury, L. B. Tabatabai, C. Liao, J. Shinar, In *Chemical and Biological Sensors for Industrial and Environmental Security*, (Eds. Arthur J. Sedlacek III, Steven D. Christensen, Roger J. Combs, Tuan Vo-Dinh), Vol. *SPIE Conference Proceedings 5994, SPIE*. Bellingham, WA, USA **2005**, 59940E.

[11] R. Liu, Y. Cai, J. M. Park, K. M. Ho, J. Shinar, R. Shinar, *Adv. Funct. Mater.* **2011**, *21*, 4744.
[12] X. D. Wang, O. S. Wolfbeis, *Chem. Soc. Rev.* **2014**, *43*, 3666.
[13] G. Williams, C. Backhouse, H. Aziz, *Electronics* **2014**, *3*, 43.
[14] S. Camou, M. Kitamura, J. P. Gouy, H. Fujita, Y. Arakawa, T. Fujii, In *Proc. SPIE 4833, Applications of Photonic Technology* **2003**, *5*, 1.
[15] B. Yao, G. Luo, L. Wang, Y. Gao, G. Lei, K. Ren, L. Chen, Y. Wang, Y. Hu, Y. Qiu, *Lab Chip* **2005**, *5*, 1041.
[16] K. N. Ren, Q. L. Liang, B. Yao, G. O. Luo, L. D. Wang, Y. Gao, Y. M. Wang, Y. Qiu, *Lab Chip* **2007**, *7*, 1574.
[17] B. Yao, H. Yang, Q. Liang, G. Luo, L. Wang, K. Ren, Y. Gao, Y. Wang, Y. Qiu, *Anal. Chem.* **2006**, *78*, 5845.
[18] L. Scholer, K. Seibel, K. Panczyk, M. Bohm, *Microelectron. Eng.* **2009**, *86*, 1502.
[19] E. Kraker, A. Haase, B. Lamprecht, G. Jakopic, C. Konrad, S. Köstler, *Appl. Phys. Lett.* **2008**, *92*, 033302.
[20] P. Puligundla, J. Jung, S. Ko, *Food Control* **2012**, *25*, 328.
[21] M. Scholles, L. Kroker, U. Vogel, J. Krüger, R. Walczak, J. Ruano-Lopez, in *Proc. /SPIE* **2010**, *7593*, 75930C.
[22] A. Marcello, D. Sblattero, C. Cioarec, P. Maiuri, P. Melpignano, *Biosens. Bioelectron.* **2013**, *46*, 44.
[23] F. So, J. Kido, P. Burrows, *MRS Bull.* **2008**, *33*, 663.
[24] G. Gu, S. R. Forrest, *IEEE J. Sel. Top. Quant. Electron.* **1998**, *4*, 83.
[25] T. Yu, W. Su, W. Li, R. Hua, B. Chu, B. Li, *Solid State Electron.* **2007**, *51*, 894.
[26] C. F. Qiu, L. D. Wang, H. Y. Chen, M. Wong, H. S. Kwok, *Appl. Phys. Lett.* **2001**, *79*, 2276.
[27] L. Zou, V. Savvate'ev, J. Booher, C. H. Kim, J. Shinar, *Appl. Phys. Lett.* **2001**, *79*, 2282.
[28] Y. Q. Li, J. X. Tang, Z. Y. Xie, L. S. Hung, S. S. Lau, *Chem. Phys. Lett.* **2004**, *386*, 128.
[29] P. E. Burrows, V. Khalfin, G. Gu, S. R. Forrest, *Appl. Phys. Lett.* **1998**, *73*, 435.
[30] R. Liu, C. Xu, R. Biswas, J. Shinar, R. Shinar, *App. Phys. Lett.* **2011**, *99*, 093305.
[31] H. Kautsky, *Biochem. Z.* **1937**, *291*, 271.
[32] R. Liu, Z. Ye, J. M. Park, M. Cai, Y. Chen, K.-M. Ho, R. Shinar, J. Shinar, *Opt. Express* **2011**, *19*, A1272.
[33] A. K. Bansal, W. Holzer, A. Penzkofer, T. Tsuboi, *Chem. Phys.* **2006**, *330*, 118.
[34] R. Biswas, C. Xu, W. Zhao, R. Liu, R. Shinar, J. Shinar, *J. Photon. Energy* **2011**, *1*, 011016.
[35] M. Kang, I. Kim, M. Chu, S. W. Kim, *J. Korean Phys. Soc.* **2011**, *59*, 3280.
[36] H. Peng, J. Sun, X. Zhu, X. Yu, M. Wong, H. S. Kwok, *Appl. Phys. Lett.* **2006**, *88*, 073517.
[37] N. Ahmad, J. Stokes, N. A. Fox, M. Teng, M. J. Cryan, *Nano Energy* **2012**, *1*, 777.
[38] Refractive Index data base of elements and compounds, http://refractiveindex.info/legacy
[39] R. Liu, Z. Gan, R. Shinar, J. Shinar, *Phys. Rev. B* **2011**, *83*, 245302.
[40] K. S. Nalwa, Y. Cai, A. L. Thoeming, J. Shinar, R. Shinar, S. Chaudhary, *Adv. Mater.* **2010**, *22*, 4157.
[41] B. Huang, S. A. Jones, B. Brandenburg, X. Zhuang, *Nat. Methods* **2008**, *5*, 1047.
[42] E. Palik, *Handbook of the Optical Constants of Solids II*, Academic Press, Boston, **1991**.
[43] F. Hamelmann, A. Brechling, A. Aschentrup, U. Heinzmann, P. Jutzi, J. Sandrock, U. Siemeling, T. Ivanova, A. Szekeres, K. Gesheva, *Thin Solid Films* **2004**, *446*, 167.
[44] S. Hermann, O. D. Gordon, M. Friedrich, D. R. T. Zahn, *Phys. Status Solidi C* **2005**, *2*, 4037.